Supporting Information

Chiral 0D hybrid lead-bromide perovskite with strong nonlinear chiroptical properties

Huan Yang,[a] Bing Sun,*[a] Junjie Guan,[b] Shun-Da Wu,[a] Peihan Wang,[b] Qiang Wang,[a] Jialiang Xu*[b] and Hao-Li Zhang*[a]

[a] State Key Laboratory of Applied Organic Chemistry (SKLAOC), Key Laboratory of Special Function Materials and Structure Design (MOE), College of Chemistry and Chemical Engineering, Lanzhou University, Lanzhou 730000, P. R. China.

[b] School of Materials Science and Engineering, Smart Sensing Interdisciplinary Science Center, Frontiers Science Center for New Organic Matter, Nankai University, 300350 Tianjin, P. R. China.

Email: bingsun@lzu.edu.cn; jialiang.xu@nankai.edu.cn; haoli.zhang@lzu.edu.cn

1. Experimental Section

Materials. *R*-3-Aminopiperidine dihydrochloride (*R*-APD·2HCl, Innochem, 98%), *S*-3-Aminopiperidine dihydrochloride (*S*-APD·2HCl, Innochem, 97%), 1*R*,2*R*-diaminocyclohexane (1*R*,2*R*-DACH, Innochem, 98%), 1*S*,2*S*-diaminocyclohexane (1*S*,2*S*-DACH, Innochem, 98%), Hydrobromic acid (HBr, ≥48% in H_2O, AR, KESHI), lead (II) acetate ($Pb(OAc)_2 \cdot 3H_2O$, Innochem, 99.5%), lead (II) oxide (PbO, Alfa Aesar, 99.99%), lead (II) bromide ($PbBr_2$, Aladdin, 99.0%) all reagents and solvents were used without further purification.

Synthesis of (*R*-/*S*-APD)$PbBr_4$ single crystals. (*R*-/*S*-APD)$PbBr_4$ was prepared with stoichiometric quantities of $(Pb(OAc)_2 \cdot 3H_2O$ (1 mmol, 379 mg) and *R*-/*S*-APD·2HCl (1 mmol, 187.19 mg) in HBr solution (4 mL). After obtaining a clear solution by heating the mixture at 120 °C and stirring for 30 min. And the colorless platelike crystals of (*R*-/*S*-APD)$PbBr_4$ were obtained at room temperature overnight. The crystals were washed with cold diethyl ether.

Synthesis of (1*R*,2*R*-/1*S*,2*S*-DACH)$_2PbBr_6 \cdot 2H_2O$ single crystals. (1*R*,2*R*-/1*S*,2*S*-DACH)$_2PbBr_6 \cdot 2H_2O$ was prepared with an amount of PbO (2 mmol, 466 mg) powder dissolved in HBr solution (6.0 mL). After obtaining a clear solution by heating the mixture at 120 °C and stirring for 30 min. And then the 1*R*,2*R*-/1*S*,2*S*-DACH (2 mmol, 228 mg) was added to the solution. The needle-like white crystals of (1*R*,2*R*-/1*S*,2*S*-DACH)$_2PbBr_6 \cdot 2H_2O$ were obtained at room temperature overnight.

Synthesis of bulk single crystals of (*R*-/*S*-APD)$PbBr_4$ and (1*R*,2*R*-/1*S*,2*S*-DACH)$_2PbBr_6 \cdot 2H_2O$. *R*-/*S*-APD·2HCl (4.15 mmol, 718 mg) and $PbBr_2$ (4.15 mmol, 1550 mg) were dissolved in 30.0 mL of HBr solution at 65 °C under constant stirring and formed a pale yellow transparent solution. The solution was filtered with a 0.2 μm Teflon syringe filter after cooling to room temperature. Block-shaped colorless (*R*-/*S*-APD)$PbBr_4$ single crystals were grown in an ambient atmosphere for about several weeks. The same method was used to prepare the bulk single crystals of (1*R*,2*R*-/1*S*.2*S*-

DACH)$_2$PbBr$_6$·2H$_2$O.

Characterization. Powder X-ray diffraction (PXRD) experiments were carried out using a Rigaku Ultima IV X-ray diffraction instrument in the 2θ between 5° and 50° with a step size of 0.02° under Cu Kα radiation (λ = 1.541871 Å). Single crystal X-ray diffraction (SCXRD) measurements were performed using a XtaLAB Synergy R, DW system, HyPix diffractometer under Mo Kα (λ = 0.71073). The single crystal structures were determined using the SHELXT methods with Olex2 program1. Thermogravimetric analyses (TGA) patterns were obtained using a Linseis STA PT1600 under N_2 atmosphere in the temperature range of 25 to 800 ℃, with a heating rate of 10 ℃/min. UV-vis absorption spectra were collected using a UV-vis spectrophotometer (UV 2600). Solid-state circular dichroism (CD) spectra were acquired using a JASCO J-1500 CD spectrometer. The perovskite sample was ground into powder. The samples for CD measurement were prepared though pressing the chiral perovskite powder and KBr powder (chiral perovskite: KBr = 1:100, w:w) into a pellet.

Second Harmonic Generation (SHG) Measurements. The SHG measurements of chiral perovskites were examined by using a home-built multiphoton nonlinear optical microscope system with a femtosecond pump (Mai Tai HP, 100 fs, 80 MHz, wavelength ranging from 690 to 1040 nm) in reflection geometry. The measurements were conducted under a reflection geometry at a 45°angle of both incidence and detection. The linearly polarized and circularly polarized pumps were altered with the λ/2 and λ/4 plates, respectively. For linear polarization-resolved SHG measurement, a λ/2 waveplate and an analyzer were respectively placed in the incident and output light path. For circular polarization-resolved SHG measurements, the λ/2 waveplate was replaced by a λ/4 waveplate and placed in the incident light path to modulate its polarization between LCP and RCP states. The power-dependent SHG measurements were completed by collecting the SHG signal intensity with increasing laser power upon laser excitation at specific wavelengths. When at a certain laser power, the SHG

intensity begins to deviate from the well-fitted quadratic relationship or drop. This power has been hence identified as the laser damage threshold (LDT) of the single crystal. The LDT was defined as LDT = P/(F × $\pi r^2 t$), where *P*, denoted incident power when the SHG signal is offset from the square dependence, *F*, *r* and *t* are frequency and radius of laser spot, pulse width, respectively. The laser spot was ~20 μm in diameter. The pulse width was ~100 fs. The frequency was 80 MHz. The second-order NLO susceptibility of the chiral perovskites was determined by using Y-cut quartz with a d_{eff} of 0.3 pm/V as the reference.

Theoretical Calculations. The DFT calculations were performed using the program VASP (Vienna Ab Initio Simulation Package)5.4.4, and the raw data was analyzed by vaspkit 1.4.1. We used the GGA-PBE function to describe the exchange correlation. A 400 eV kinetic energy cutoff and a 4 × 3 × 2 for (*R*-/*S*-APD)$PbBr_4$ / 3 × 3 × 1 for (1*R*,2*R*-/1*S*,2*S*-DACH)$_2PbBr_6 \cdot 2H_2O$gamma-centered K sampling grid were used for integration. The structures are firstly fully relaxed until the Hellmann–Feynmann force on each atom and the total energy difference between neighboring loops reach 10^{-6} eV and 0.02 eV·Ang^{-1} within 500 loops limitation. For the band structure, the K-Path was generated by vaspkit 1.4.1. Besides DOS, the PDOS (projected density of states) has been also calculated. PDOS is calculated as projected DOS, where the information about the different contributions of the different elements is computed.

2. Characterization

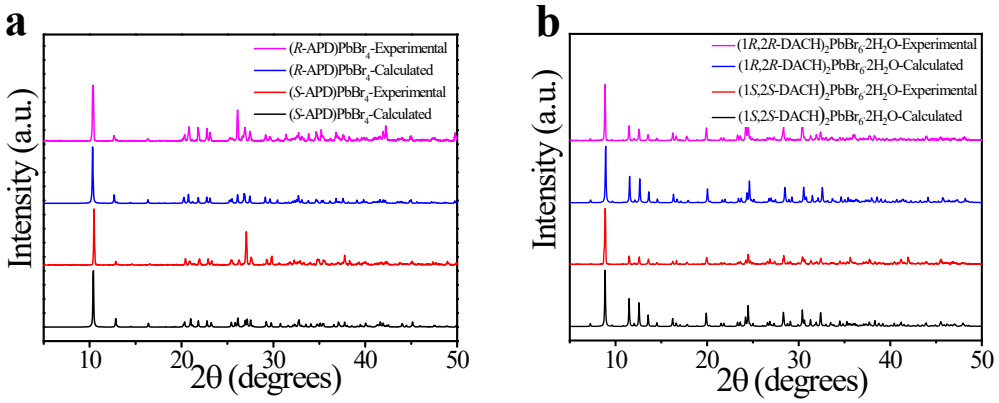

Figure S1. Experimental and calculated powder X-ray diffraction (PXRD) patterns of **a.** (*R*-/*S*-APD)$PbBr_4$ and **b.** (1*R*,2*R*-/1*S*,2*S*-DACH)$_2PbBr_6 \cdot 2H_2O$.

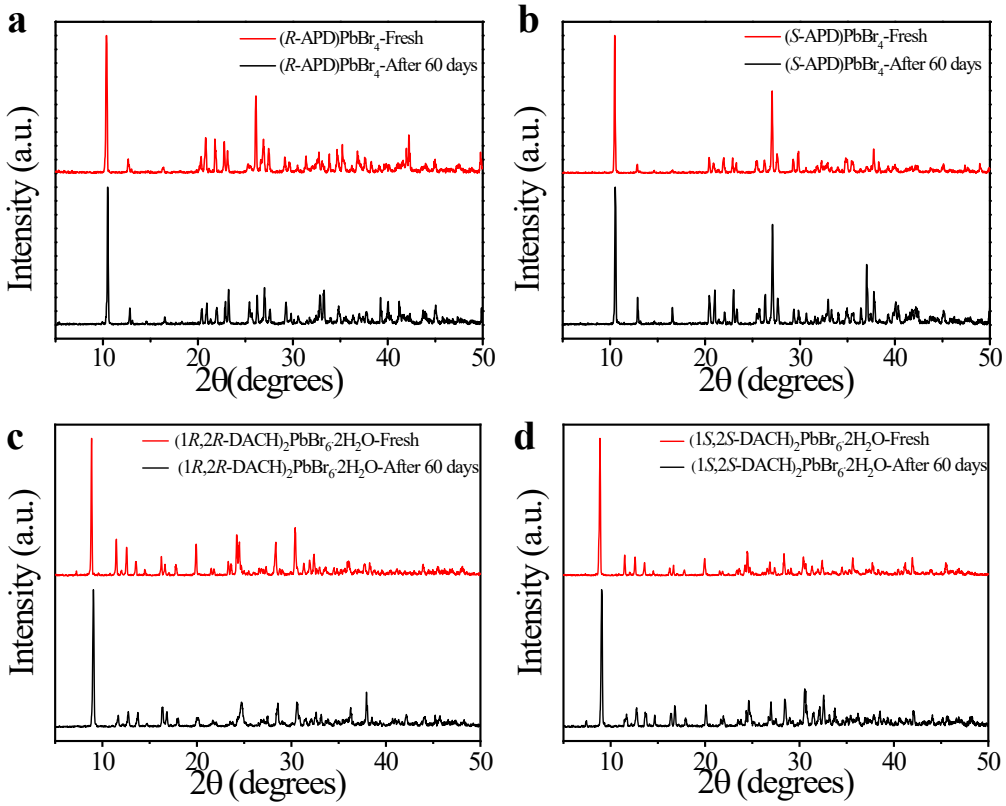

Figure S2. Powder X-ray diffraction (PXRD) patterns of the as-prepared and exposed in the air after 60 days. **a.** (*R*-APD)$PbBr_4$, **b.** (*S*-APD)$PbBr_4$, **c.** (1*R*,2*R*-DACH)$_2PbBr_6 \cdot 2H_2O$, **d.** (1*S*,2*S*-DACH)$_2PbBr_6 \cdot 2H_2O$.

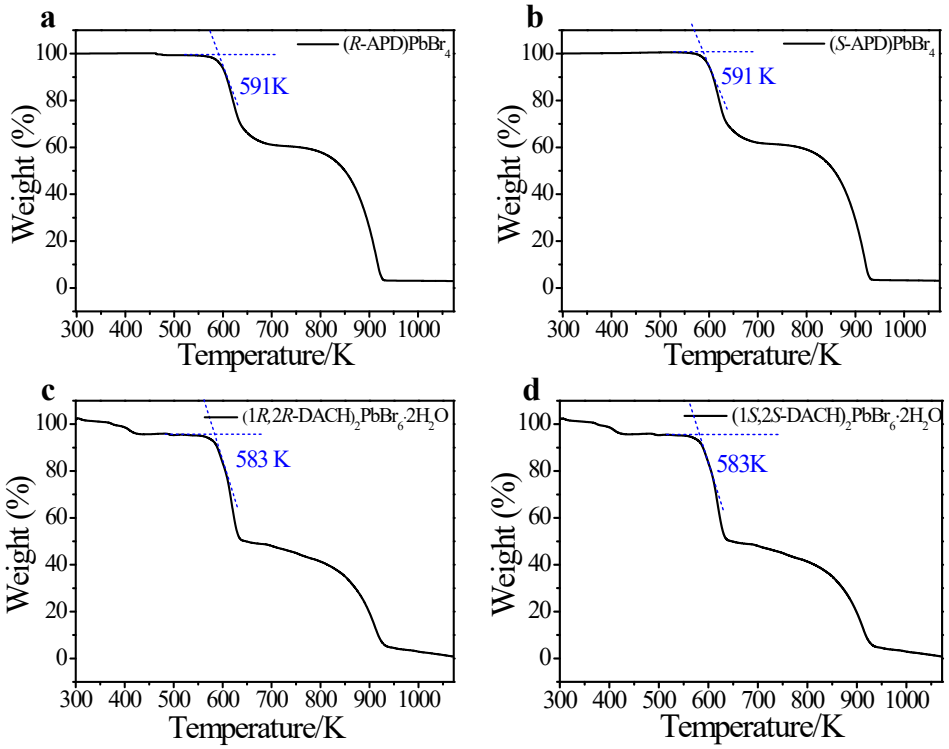

Figure S3. Thermal stability of **a.** (*R*-APD)$PbBr_4$, **b.** (*S*-APD)$PbBr_4$, **c.** (1*R*,2*R*-DACH)$_2PbBr_6 \cdot 2H_2O$ and **d.** (1*S*,2*S*-DACH)$_2PbBr_6 \cdot 2H_2O$, was measured by the thermogravimetric analysis (TGA) method.

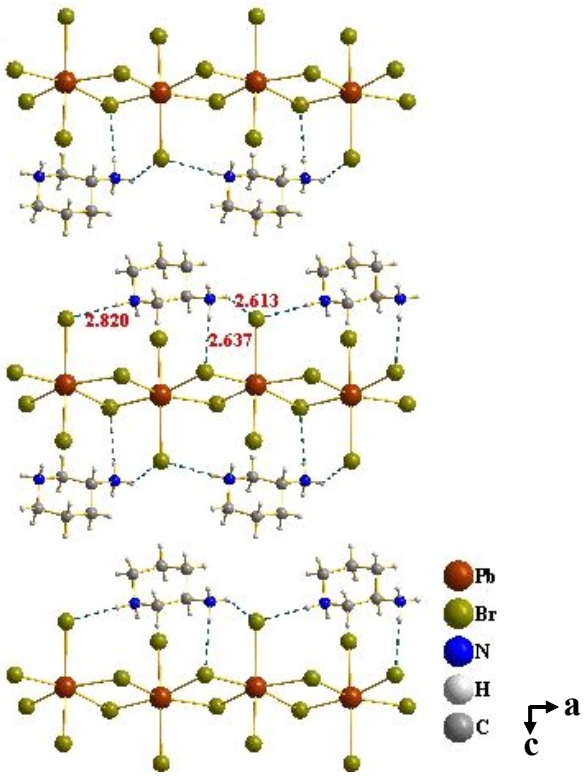

Figure S4. The hydrogen bonding N-H···Br of (*R*-APD)$PbBr_4$, which are marked by the dotted blue lines.

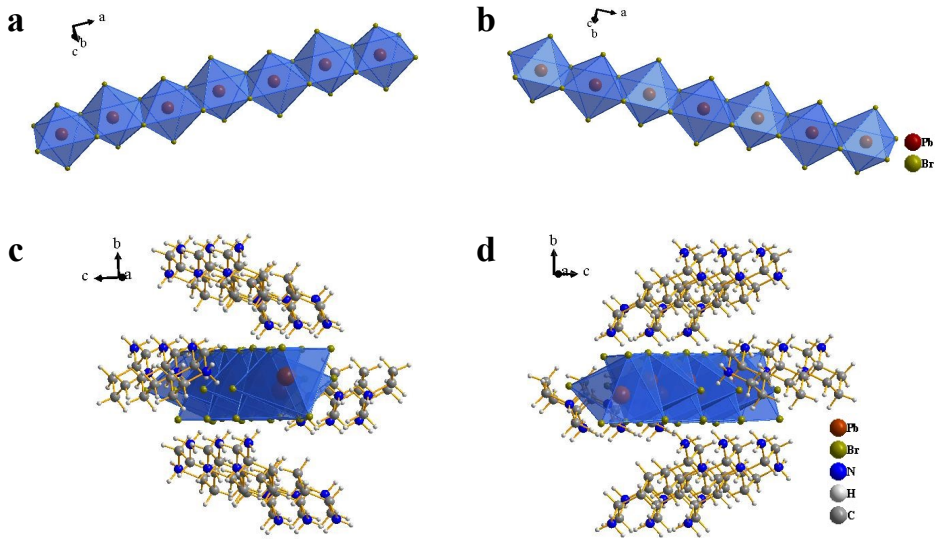

Figure S5. a. View of the individual inorganic chain based on edge-shared $[PbBr_6]^{4-}$ octahedrons of (*R*-APD)$PbBr_4$. **b.** View of the individual inorganic chain based on edge-shared $[PbBr_6]^{4-}$ octahedrons of (*S*-APD)$PbBr_4$. **c.** View of an individual one-dimensional inorganic chain wrapped by the organic cations of (*R*-APD)$PbBr_4$. **d.** View of an individual one-dimensional inorganic chain wrapped by the organic cations of (*S*-APD)$PbBr_4$.

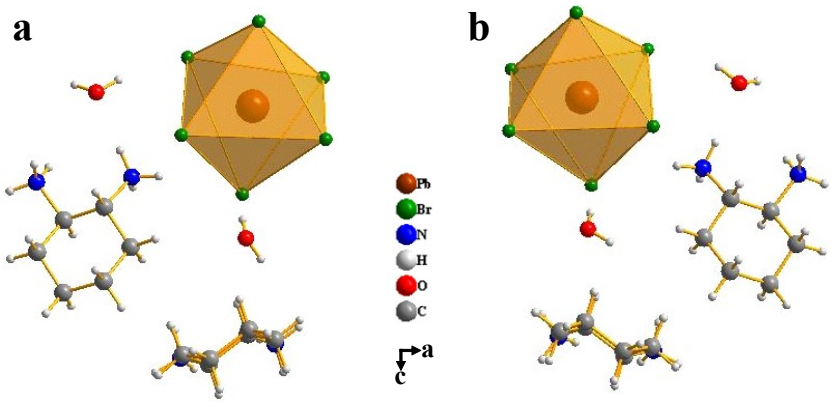

Figure S6. The asymmetry unit of **a.** (1*R*,2*R*-DACH)$_2PbBr_6 \cdot 2H_2O$ and **b.** (1*S*,2*S*-DACH)$_2PbBr_6 \cdot 2H_2O$ as viewed from the *b*-axis.

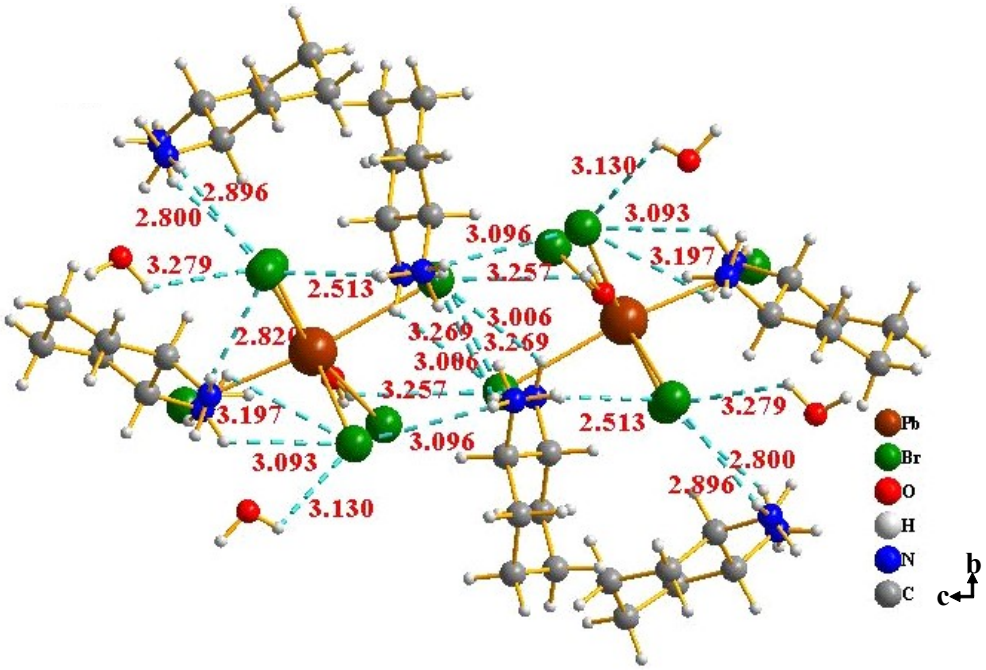

Figure S7. The hydrogen bonding N-H···Br and O-H···Br of (1*R*,2*R*-DACH)$_2$PbBr$_6$·2H$_2$O, which are marked by the dotted blue lines.

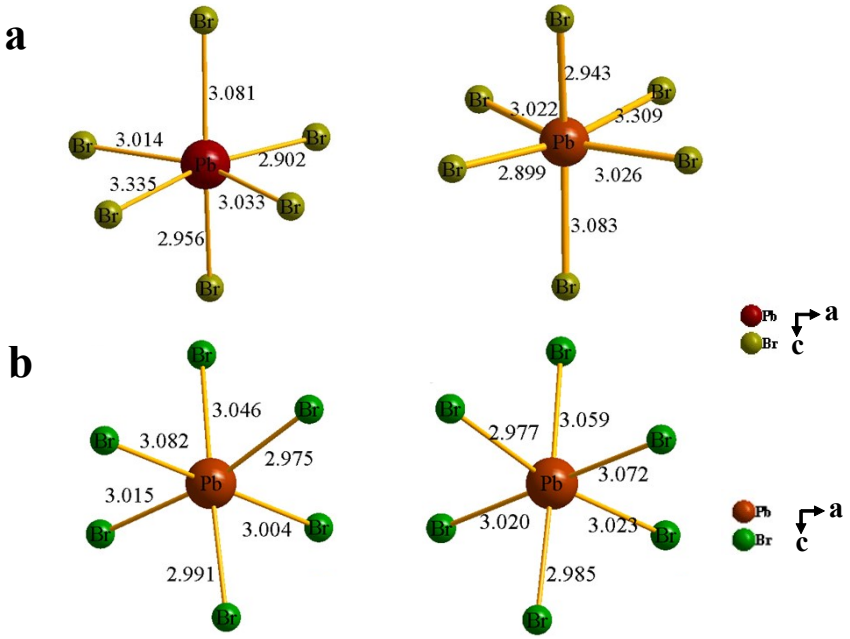

Figure S8. a. The distorted [PbBr$_6$]$^{4-}$ structure of (*R*-APD)PbBr$_4$ (left) and (*S*-APD)PbBr$_4$ (right). **b.** The distorted [PbBr$_6$]$^{4-}$ structure of (1*R*,2*R*-DACH)$_2$PbBr$_6$·2H$_2$O (left) and (1*S*,2*S*-DACH)$_2$PbBr$_6$·2H$_2$O (right).

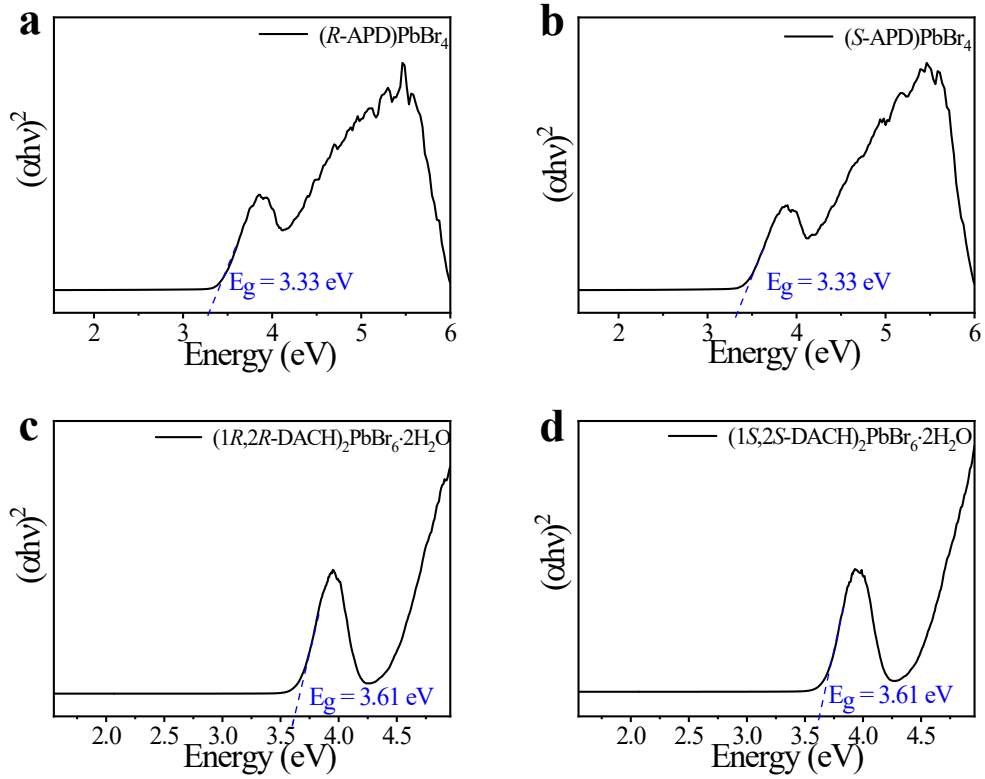

Figure S9. The corresponding Tauc plots of **a.** (*R*-APD)$PbBr_4$, **b.** (*S*-APD)$PbBr_4$, **c.** (1*R*,2*R*-DACH)$_2PbBr_6 \cdot 2H_2O$ and **d.** (1*S*,2*S*-DACH)$_2PbBr_6 \cdot 2H_2O$, respectively.

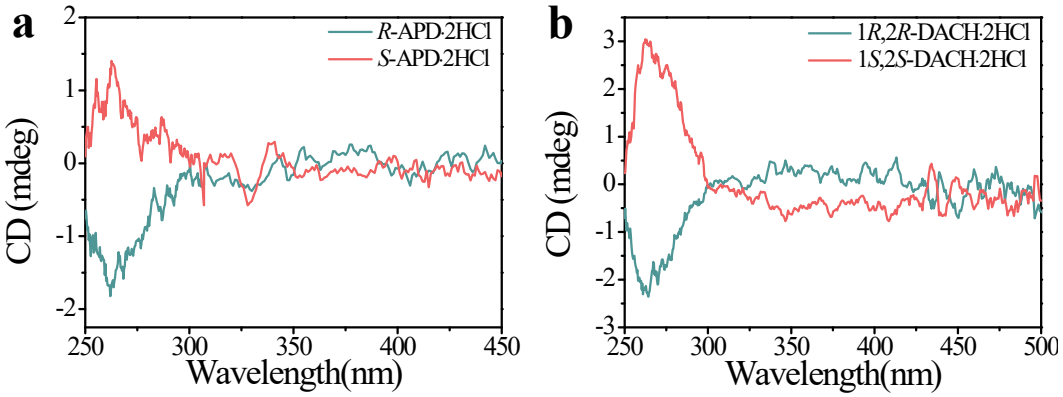

Figure S10. a. Circular dichroism spectra of *R*-APD·2HCl and *S*-APD·2HCl . **b.** Circular dichroism spectra of 1*R*,2*R*-DACH·2HCl and 1*S*,2*S*-DACH·2HCl.

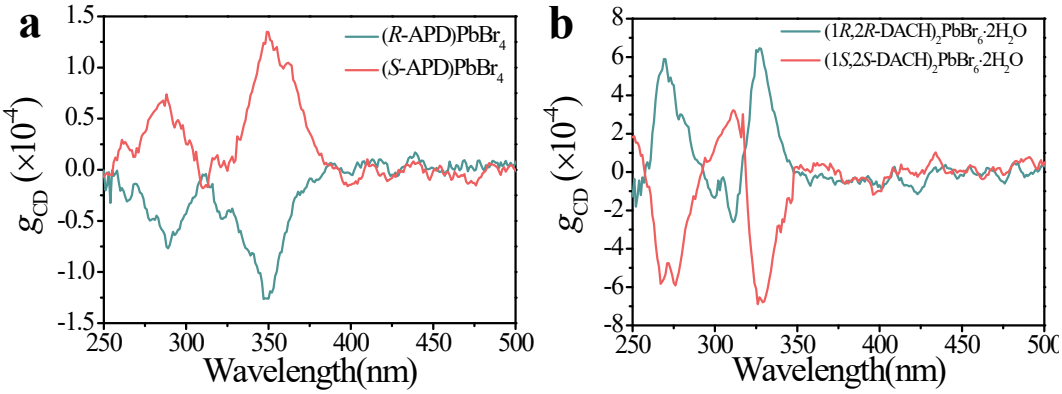

Figure S11. The g_{CD} spectra of **a.** (*R*/*S*-APD)$PbBr_4$ and **b.** (1*R*,2*R*/1*S*,2*S*-DACH)$_2PbBr_6 \cdot 2H_2O$, respectively.

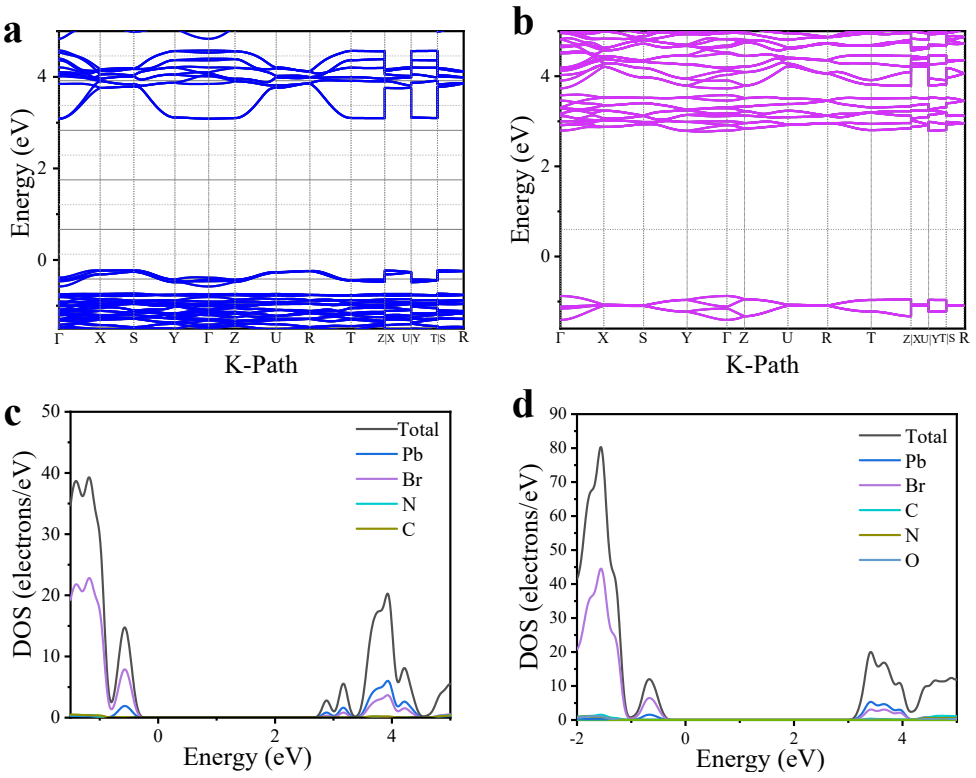

Figure S12. a-b. Calculated electronic band structures of (*R*-APD)$PbBr_4$ and (1*R*,2*R*-DACH)$_2PbBr_6 \cdot 2H_2O$. **c-d.** Calculated partial DOS of (*R*-APD)$PbBr_4$ and (1*R*,2*R*-DACH)$_2PbBr_6 \cdot 2H_2O$.

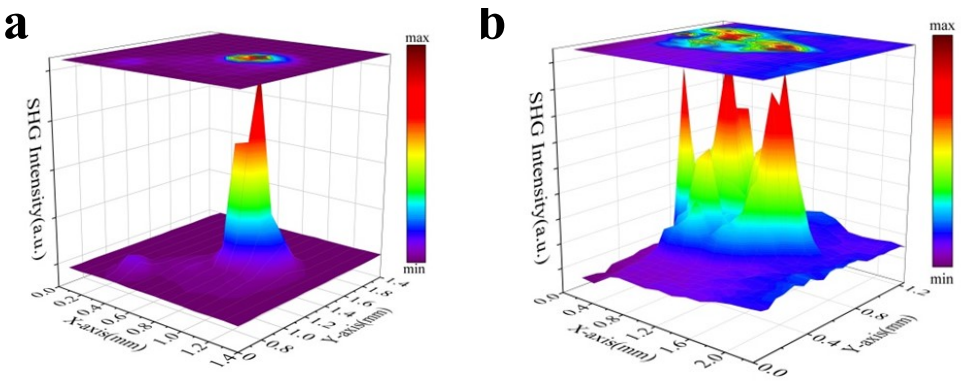

Figure S13. a. The scanned image of (*S*-APD)$PbBr_4$ crystal by detecting the SHG signal at 520 nm when pumped 1040 nm. The scanned area is 2.0 × 1.2 mm^2. **b.** The scanned image of (1*S*,2*S*-DACH)$_2PbBr_6 \cdot 2H_2O$ crystal by detecting the SHG signal at 440 nm when pumped at 880 nm. The scanned area is 2.0 × 1 mm^2.

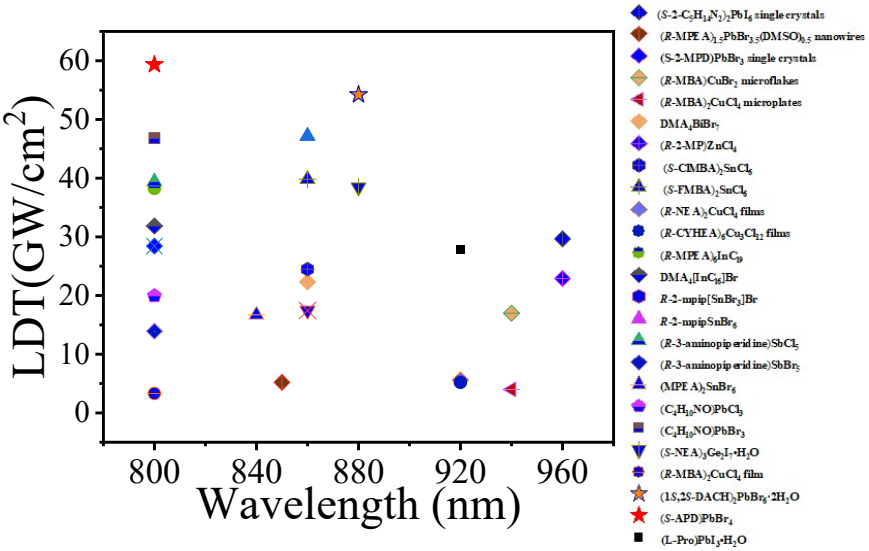

Figure S14. Comparison of LDT of chiral metal halides in literatures and this work.

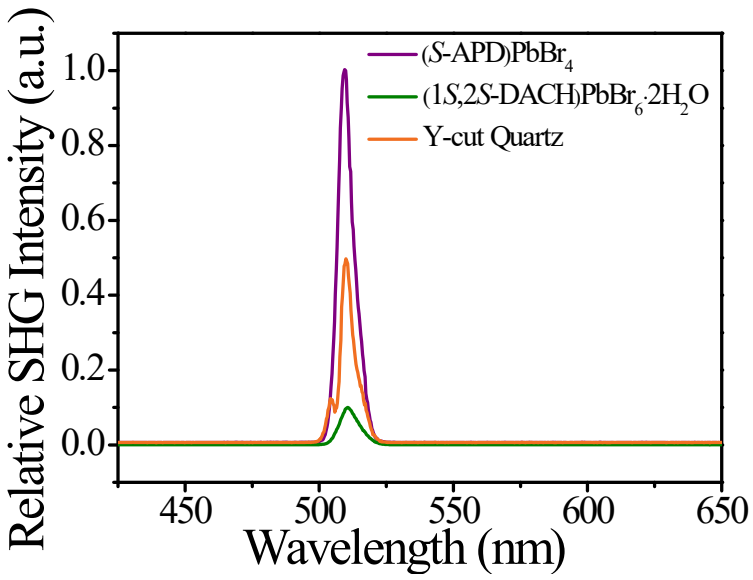

Figure S15. The comparison of SHG signal intensities of (*S*-APD)$PbBr_4$ and (1*S*,2*S*-DACH)$_2PbBr_6 \cdot 2H_2O$ crystals and Y-cut quartz at 1020 nm under the same test conditions.

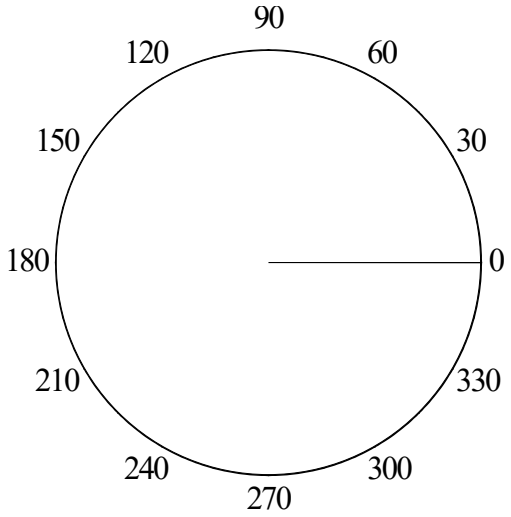

Figure S16. Polarization dependence of the SHG intensity of (*S*-APD)$PbBr_4$ crystal as a function of the linear polarization angle pumped at 1040 nm. The purple line is the nonlinear fitting of data points.

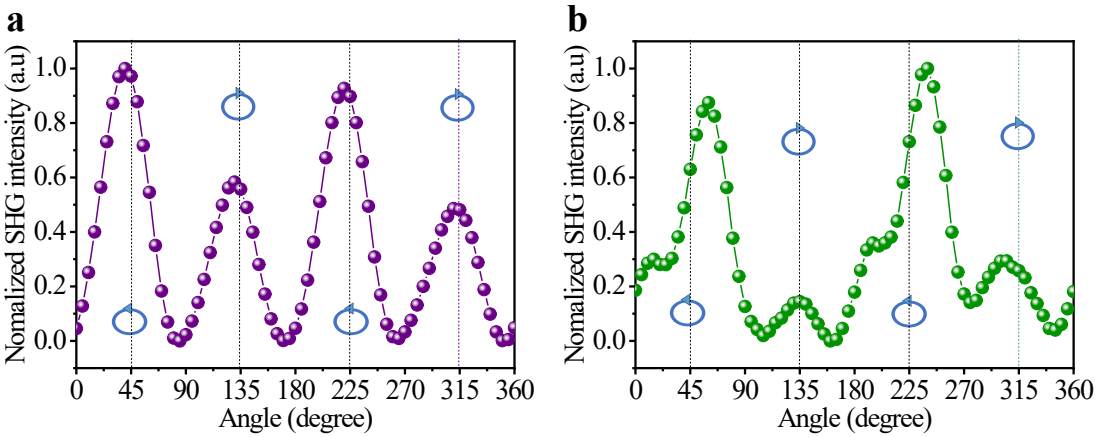

Figure S17. a-b. The SHG intensity of (*R*-APD)$PbBr_4$ and (1*R*,2*R*-DACH)$_2PbBr_6 \cdot 2H_2O$ crystals at various elliptic polarized angles pumped at 1040 nm laser, respectively. The laser is left-handed circularly polarized when the rotation angle is 45 and 225°, while it is right-handed circularly polarized at 135 and 315°, as indicated by the blue arrows. It is noted that the experimental observed SHG-CD spectra can vary significantly when measured at different spots on the same crystal plane, which may be attribute to the anisotropy of the crystal surface. Unless otherwise noted, the SHG-CD results reported herein represents that acquired under optimal condition.

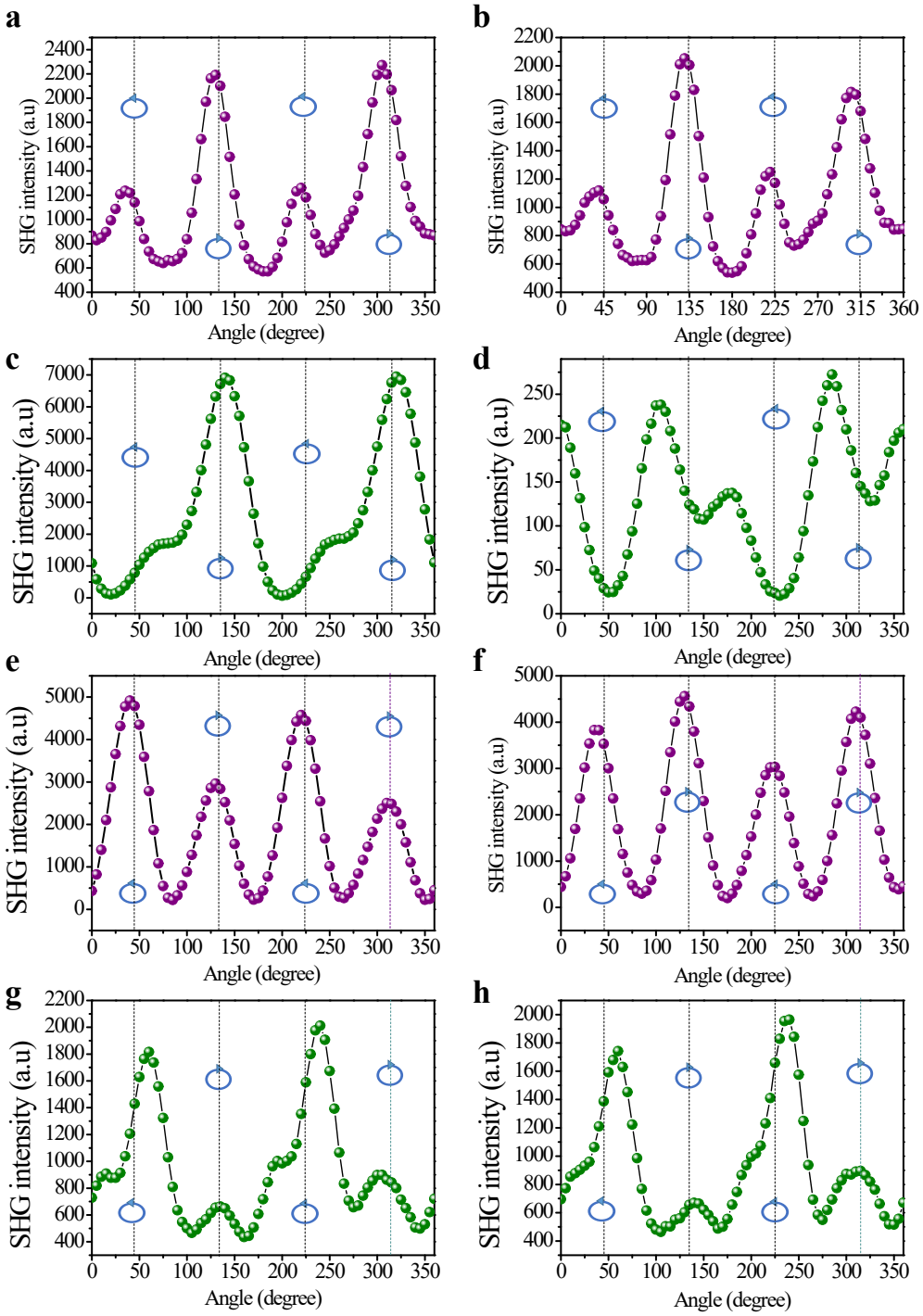

Figure S18. Summary of SHG-CD intensity at various elliptic polarized angles measured on different crystals. **a.** and **b.** The SHG-CD intensity of (*S*-APD)$PbBr_4$ crystals with thicknesses of ~200 and ~500 μm, respectively. **c.** and **d.** The SHG-CD intensity of (1*S*,2*S*-DACH)$_2PbBr_6 \cdot 2H_2O$ crystals with thicknesses of ~200 and ~400 μm, respectively. **e.** and **f.** The SHG-CD intensity of (*R*-APD)$PbBr_4$ crystals with thicknesses of ~250 and ~500 μm, respectively. **g.** and **h.** The SHG-CD intensity of (1*R*,2*R*-DACH)$_2PbBr_6 \cdot 2H_2O$ crystals with thicknesses of ~300 and ~500 μm, respectively. It is noted that Figures S18a, S18c, S18e and S18g corresponding to Figure 5c, Figure 5d, Figure S17a and Figure S17b, were used only for comparison of the SHG-CD intensity of different crystals.

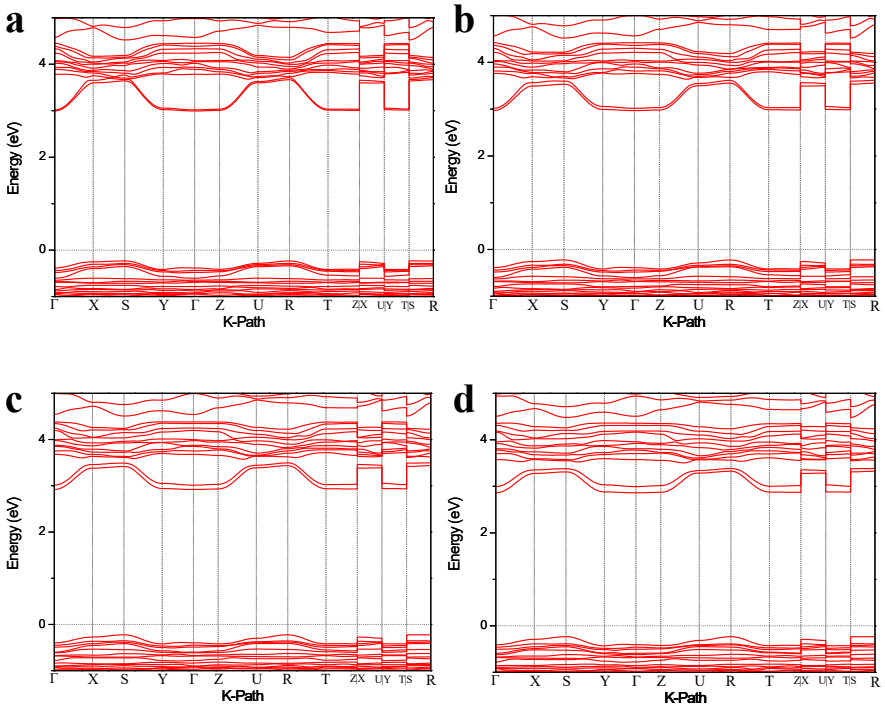

Figure S19. Electro-phonon renormalized band gaps of (*S*-APD)PbBr$_4$. Calculated band structure considering the effect of electron-phonon coupling at 0 K (a), 100 K (b), 200 K (c) and 300 K (d). The electron-phonon interactions from ZG displacements were generated accounting for thermal lattice expansion.

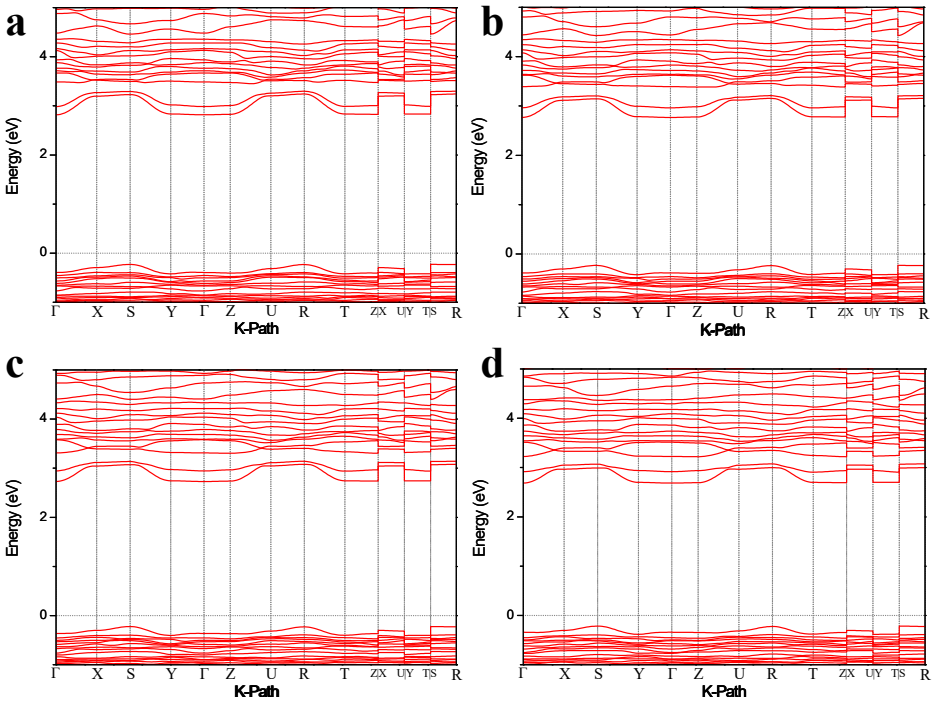

Figure S20. Electro-phonon renormalized band gaps of (*S*-APD)PbBr$_4$. Calculated band structure considering the effect of electron-phonon coupling at 400 K (a), 500 K (b), 600 K (c) and 700 K (d). The electron-phonon interactions from ZG displacements were generated accounting for thermal lattice expansion.

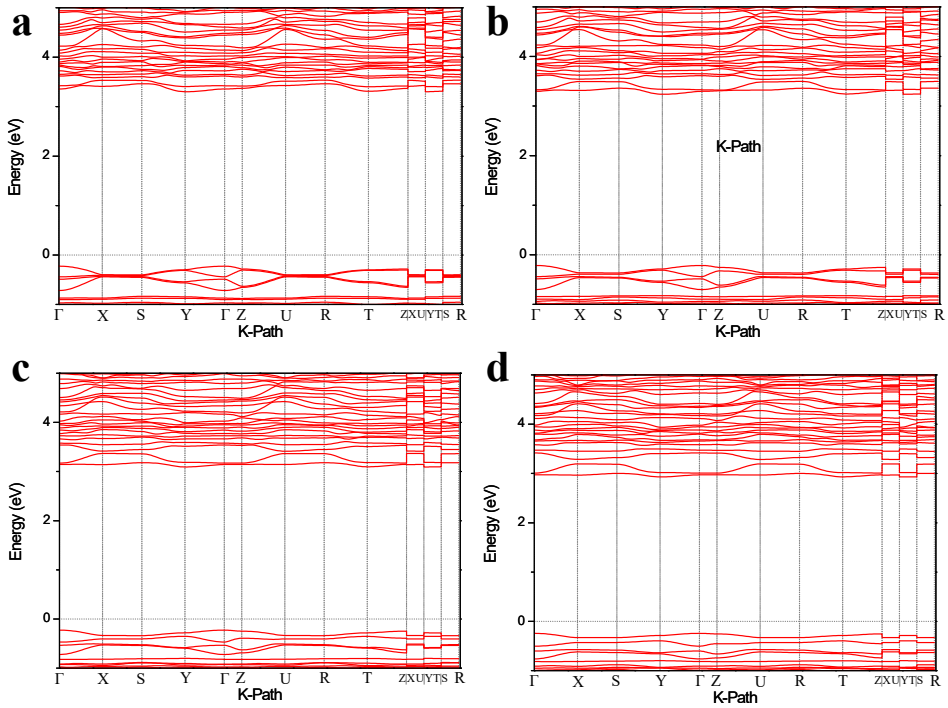

Figure S21. Electro-phonon renormalized band gaps of (1*S*,2*S*-DACH)$_2$PbBr$_6$·2H$_2$O. Calculated band structure considering the effect of electron-phonon coupling at 0 K (a), 100 K (b), 200 K (c) and 300 K (d). The electron-phonon interactions from ZG displacements were generated accounting for thermal lattice expansion.

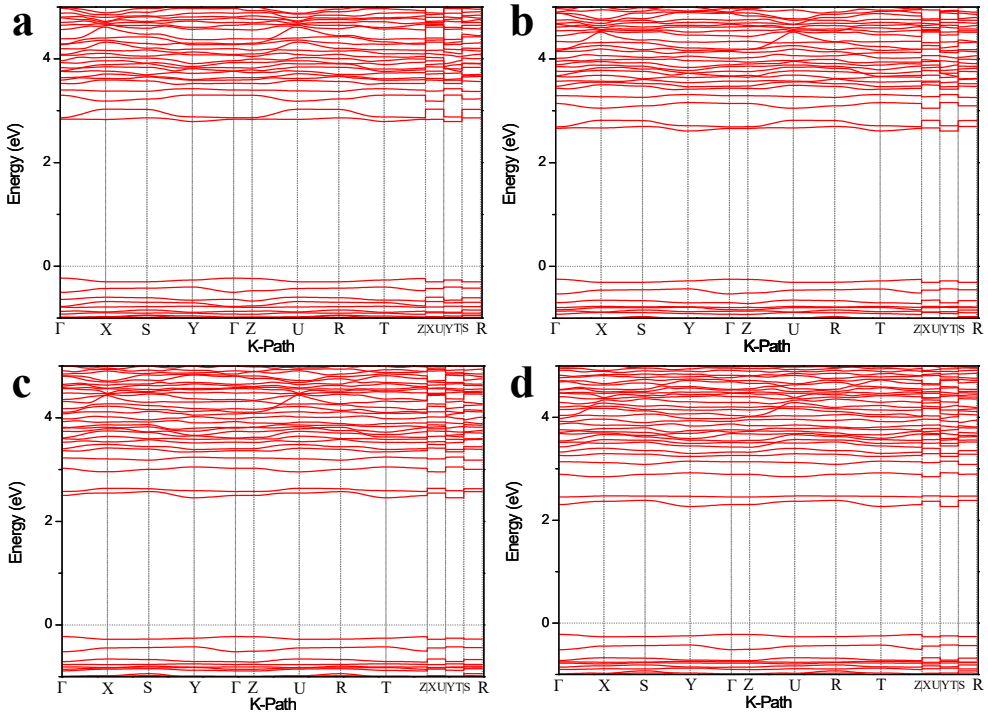

Figure S22. Electro-phonon renormalized band gaps of (1*S*,2*S*-DACH)$_2$PbBr$_6$·2H$_2$O. Calculated band structure considering the effect of electron-phonon coupling at 400 K (a), 500 K (b), 600 K (c) and 700 K (d). The electron-phonon interactions from ZG displacements were generated accounting for thermal lattice expansion.

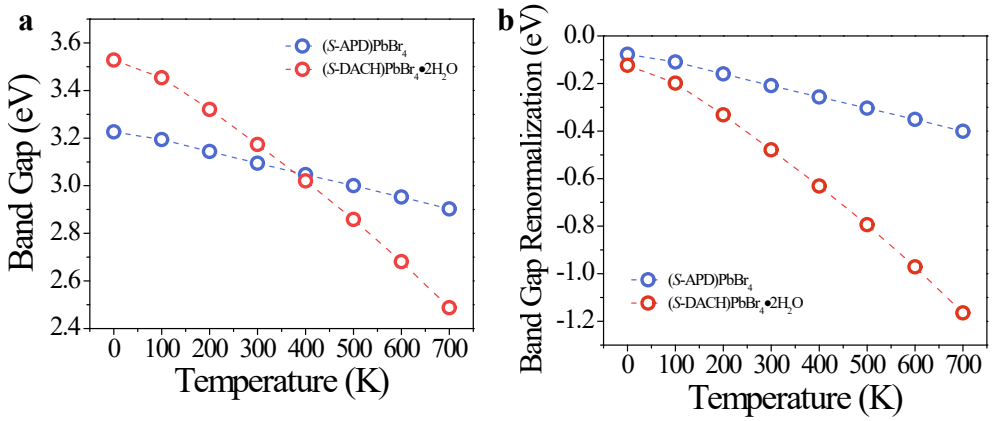

Figure S23. Electro-phonon renormalized band gaps of (*S*-APD)PbBr$_4$ and (1*S*,2*S*-DACH)$_2$PbBr$_6$·2H$_2$O. Phonon-induced band gap renormalization of (*S*-APD)PbBr$_4$ (blue) and (1*S*,2*S*-DACH)$_2$PbBr$_6$·2H$_2$O (red).

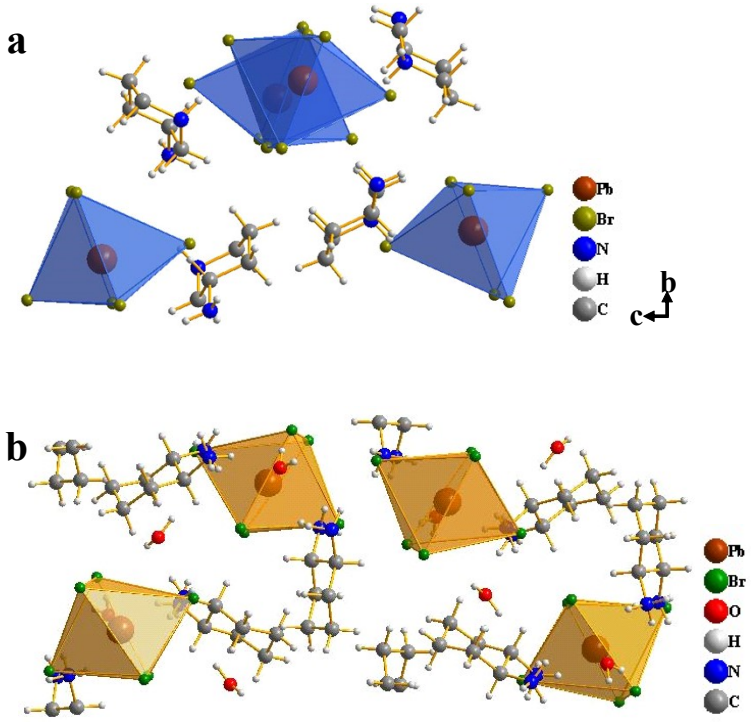

Figure S24. a. The unite cell structure of (*S*-APD)PbBr$_4$. **b.** The unite cell structure of (1*S*,2*S*-DACH)$_2$PbBr$_6$·2H$_2$O.

Table S1. Crystal data and structure refinement of (*R*-/*S*-APD)$PbBr_4$.

CCDC	2339434	2339435
Identification code	(*R*-APD)$PbBr_4$	(*S*-APD)$PbBr_4$
Empirical formula	$C_5H_{14}N_2PbBr_4$	$C_5H_{14}N_2PbBr_4$
Formula weight,g·mol^{-1}	629.01	629.01
Temperature (K)	300	150
Crystal system	orthorhombic	orthorhombic
Space group	$P2_12_12_1$	$P2_12_12_1$
a (Å)	8.7802(2)	8.7810(3)
b (Å)	10.8321(3)	10.8005(4)
c (Å)	13.9609(4)	13.7783(5)
α (°)	90	90
β (°)	90	90
γ (°)	90	90
V (Å^3)	1327.79(6	1306.72(8)
Z	4	4
ρ (calculated) (g/cm^3)	3.147	3.197
Absorption coeffcient, mm^{-1}	24.704	25.103
F (000)	1120.0	1120.0
Theta range for data collection	5.48 to 52.74	4.792 to 60.832
Index ranges	$-10 \le h \le 9$ $-13 \le k \le 13$ $-17 \le l \le 17$	$-11 \le h \le 11$ $-13 \le k \le 13$ $-15 \le l \le 19$
Reflections collected	9538	9815
Independent reflections	2707 [R_{int} = 0.0443]	3208 [R_{int} = 0.0954]
Data/restraints/parameters	2707/0/110	3208/42/110
Goodness-of-fit on F^2	1.095	1.170
Final R indices [I > 2σ(I)]	R_1 = 0.0341, wR_2 = 0.0795	R_1 = 0.0711, wR_2 = 0.1867
R indices (all data)	R_1 = 0.0368, wR_2 = 0.0804	R_1 = 0.0797, wR_2 = 0.1925
Largest diff. peak and hole, e.Å^{-3}	1.22 and -2.66	6.72 and -4.70
Flack parameter	-0.012(8)	-0.02(3)

Table S2. Crystal data and structure refinement of (1*R*,2*R*-/1*S*,2*S*-DACH)$_2$PbBr$_6$·2H$_2$O.

CCDC	2339436	2339439
Identification code	(1*R*,2*R*-DACH)$_2$PbBr$_6$·2H$_2$O	(1*S*,2*S*-DACH)$_2$PbBr$_6$·2H$_2$O
Empirical formula	$C_{12}H_{36}N_4O_2PbBr_6$	$C_{12}H_{36}N_4O_2PbBr_6$
Formula weight,g·mol^{-1}	955.10	955.10
Temperature (K)	150	293
Crystal system	orthorhombic	orthorhombic
Space group	$P2_12_12_1$	$P2_12_12_1$
a (Å)	9.8774(2)	9.9329(2)
b (Å)	10.8539(2)	10.9337(3)
c (Å)	24.3071(5)	24.3960(6)
α (°)	90	90
β (°)	90	90
γ (°)	90	90
V (Å^3)	2605.92(9)	2649.49(11)
Z	4	4
ρ (calculated) (g/cm^3)	2.434	2.394
Absorption coeffcient, mm^{-1}	15.688	23.099
F (000)	1776	1776
Theta range for data collection	4.11 to 61.462	3.624 to 67.239
Index ranges	$-10 \le h \le 13$ $-14 \le k \le 12$ $-31 \le l \le 29$	$-8 \le h \le 11$ $-12 \le k \le 13$ $-28 \le l \le 29$
Reflections collected	23794	16990
Independent reflections	6672 [R_{int} = 0.0284]	4731 [R_{int} = 0.07]
Data/restraints/parameters	6672/0/236	4731 / 0 / 231
Goodness-of-fit on F^2	1.023	1.063
Final R indices [I > 2σ(I)]	R_1 = 0.0206, wR_2 = 0.0330	R_1 = 0.0452, wR_2 = 0.1141
R indices (all data)	R_1 = 0.0249, wR_2 = 0.0336	R_1 = 0.0469, wR_2 = 0.1167
Largest diff. peak and hole, e.Å^{-3}	0.69 and -0.63	1.841 and -2.254
Flack parameter	-0.018(3)	-0.053(6)

Table S3. Bond Lengths for (*R*-/*S*-APD)$PbBr_4$.

(*R*-APD)$PbBr_4$			(*S*-APD)$PbBr_4$		
Atom	Atom	Length/Å	Atom	Atom	Length/Å
Pb1	Br2	3.0136(13)	Pb1	Br1[1]	3.026(3)
Pb1	Br2[1]	3.0334(13)	Pb1	Br1	3.021(3)
Pb1	Br3	2.9560(13)	Pb1	Br2	2.943(2)
Pb1	Br4	3.0810(14)	Pb1	Br3	2.898(3)
Pb1	Br5	2.9023(14)	Pb1	Br4	3.083(3)
Pb1	Br6	3.3350(14)	Pb1	Br5	3.309(2)

Table S4. Bond Lengths for (1*R*,2*R*-/1*S*,2*S*-DACH)$_2PbBr_6 \cdot 2H_2O$.

(1*R*,2*R*-DACH)$_2PbBr_6 \cdot 2H_2O$			(1*S*,2*S*-DACH)$_2PbBr_6 \cdot 2H_2O$		
Atom	Atom	Length/Å	Atom	Atom	Length/Å
Pb1	Br1	3.0154(5)	Pb1	Br6	2.9766(17)
Pb1	Br2	3.0463(5)	Pb1	Br1	2.9848(17)
Pb1	Br3	2.9752(5)	Pb1	Br2	3.0195(16)
Pb1	Br4	3.0039(5)	Pb1	Br5	3.0230(16)
Pb1	Br5	2.9911(5)	Pb1	Br3	3.0588(16)
Pb1	Br6	3.0820(5)	Pb1	Br4	3.0717(18)

Table S5. Octahedral distortion calculation for (*R*-/*S*-APD)$PbBr_4$ and (1*R*,2*R*-/1*S*,2*S*-DACH)$_2PbBr_6 \cdot 2H_2O$.

Octahedral Distortion	**Δ*d***
(*R*-APD)$PbBr_4$	2.05×10^{-3}
(*S*-APD)$PbBr_4$	1.86×10^{-3}
(1*R*,2*R*-DACH)$_2PbBr_6 \cdot 2H_2O$	1.4×10^{-4}
(1*S*,2*S*-DACH)$_2PbBr_6 \cdot 2H_2O$	1.34×10^{-4}

Table S6. Comparison of LDT of chiral metal halides in literatures and this work.

	Pulse width/ fs	Repetitionrate/MHz	Laser spot diameter / μm	Power/ mW	Power intensity mJ/cm²	LDT GW/cm²	Ref.
(*R*-MPEA)$_{1.5}$PbBr$_{3.5}$(DMSO)$_{0.5}$ nanowires	100	82	10	67.5	0.52	5.2	[1]
(*S*-2-C$_5$H14N$_2$)$_2$PbI$_6$ single crystals	100	80	20	745	2.97	29.66	[2]
(*S*-2-MPD)PbBr$_3$ single crystals	100	80	20	714	2.84	28.42	[3]
(*R*-MBA)CuBr$_2$ microflakes	100	82	-	-	1.7	17	[4]
(*R*-MBA)$_2$CuCl$_4$ microplates	100	82	-	-	0.4	4	[4]
DMA$_4$BiBr$_7$	100	80	20	563	2.23	22.3	[5]
(*R*-2-MP)ZnCl$_4$	100	80	20	575	2.29	22.89	[6]
(*S*-ClMBA)$_2$SnCl$_6$	100	80	20	615	2.45	24.48	[7]
(*S*-FMBA)$_2$Sn Cl$_6$	100	80	20	1000	3.98	39.81	[7]
(*R*-NEA)$_2$CuCl$_4$ films	100	80	-	-	0.56	5.6	[8]
(*R*-CYHEA)$_6$Cu$_3$Cl$_{12}$ films	100	80	-	-	0.52	5.2	[8]
(*R*-MPEA)$_6$InCl$_9$	100	80	20	961	3.82	38.26	[9]
DMA$_4$[InCl$_6$]Br	100	80	20	800	3.18	31.85	[10]
R-2-mpip[SnBr$_3$]Br	100	80	20	438	1.74	17.44	[11]
R-2-mpipSnBr$_6$	100	80	20	1185	4.72	47.17	[11]
(*R*-3-aminopiperidine)SbCl$_5$	100	80	20	961	3.94	39.4	[12]
(*R*-3-aminopiperidine)SbBr$_5$	100	80	20	350	1.39	13.93	[12]
(MPEA)$_2$SnBr$_6$	100	80	20	420	1.67	16.72	[13]
(C$_4$H$_{10}$NO)PbCl$_3$	140	80	2	-	-	19.94	[14]
(C$_4$H$_{10}$NO)PbBr$_3$	140	80	2	-	-	46.82	[14]
(*S*-NEA)$_3$Ge$_2$I$_7$·H$_2$O	100	80	6	-	-	38.46	[15]
(*R*-MBA)$_2$CuCl$_4$ film	100	80	20	-	-	3.31	[16]
(L-Pro)PbI$_3$·H$_2$O	100	80	20	700	2.8	27.87	[17]
(1*S*,2*S*-DACH)$_2$PbBr$_6$·2H$_2$O	100	80	20	1362	5.42	54.22	**This work**
(*S*-APD)PbBr$_4$	100	80	20	1491	5.94	59.36	**This work**

$$Power_{intensity} = \frac{P}{f\pi r^2}$$

$$LDT = \frac{P}{f\pi r^2 t}$$

The laser-induced damage threshold (LDT) was defined as LDT = P/(F × πr^{2}t), where P, denoted incident power when the SHG signal is offset from the square dependence, F, r and t are frequency and radius of laser spot, pulse width, respectively.

Table S7. Comparison of $g_{SHG\text{-}CD}$ in the literature and this work.

Chiral compounds	Morphology	Laser conditions	Anisotropic g factor	Ref
[(*R/S*)-3-aminopiperidine]PbI_4	single crystal	1064 nm, pulse power of 400mV	$g_{SHG\text{-}CD}$ = 0.21	[18]
(*R*-MBA)$_4Bi_2Br_{10}$	spiral microplates.	1200 nm, 100 fs, 1 kHz	$g_{SHG\text{-}CD}$ = 0.58	[19]
(*R*-MBACl)$_2PbI_4$	thin film	880 nm, 100 fs, 80MHz	$g_{SHG\text{-}CD}$= 1.57	[20]
P-DMA$_4$[$InCl_6$]Br	single crystal	1040 nm, 100 fs. 80 MHz	$g_{SHG\text{-}CD}$= 1.56	[10]
(*R*-1-(1-NEA)$_2CuCl_4$	thin film	880 nm, 100 fs, 80 MHz	$g_{SHG\text{-}CD}$ = 0.41	[21]
(*R*-1-(2-NEA)$_2CuCl_4$	thin film	880 nm, 100 fs, 80 MHz	$g_{SHG\text{-}CD}$ = 0.1	[21]
(*R/S*-MPEA)BA$PbBr_4$	thin film	800 nm, 100 fs, 80 MHz	$g_{SHG\text{-}CD}$ = 0.8	[22]
(*R*-NEA)$_3Ge_2I_7 \cdot H_2O$	single crystal	880 nm,100 fs, 80 MHz	$g_{SHG\text{-}CD}$ = 0.48	[15]
(*S*-NEA)$_3Ge_2I_7 \cdot H_2O$	single crystal	880 nm,100 fs, 80 MHz	$g_{SHG\text{-}CD}$ = 0.45	[15]
(1*S*,2*S*-DACH)$_2PbBr_6 \cdot 2H_2O$	single crystal	1040 nm,100 fs, 80 MHz	$g_{SHG\text{-}CD}$ = 1.58	This work
(*S*-APD)$PbBr_4$	single crystal	1040 nm,100 fs, 80 MHz	$g_{SHG\text{-}CD}$ = 0.60	This work

$$g_{SHG-CD} = 2\frac{I_{LCP} - I_{RCP}}{I_{LCP} + I_{RCP}}$$

where I_{LCP} and I_{RCP} represent the SHG intensities under LCP and RCP light excitation, respectively.

3. References

1. Yuan, C.; Li, X.; Semin, S.; Feng, Y.; Rasing, T.; Xu, J., Chiral Lead Halide Perovskite Nanowires for Second-Order Nonlinear Optics. *Nano Lett.* **2018,** *18* (9), 5411-5417.

2. Jia, X.; Zheng, Y.; Cheng, P.; Han, X.; Xu, L.; Xu, J., Methylpiperazine based 0D chiral hybrid lead halides for second harmonic generation. *Dalton Trans.* **2022,** *51* (18), 7248-7254.

3. Zheng, Y.; Xu, J.; Bu, X. H., 1D Chiral Lead Halide Perovskites with Superior Second-Order Optical Nonlinearity. *Adv. Opt. Mater.* **2022,** *10* (1), 2101545.

4. Ge, F.; Li, B. H.; Cheng, P.; Li, G.; Ren, Z.; Xu, J.; Bu, X. H., Chiral Hybrid Copper(I) Halides for High Efficiency Second Harmonic Generation with a Broadband Transparency Window. *Angew. Chem. Int. Ed.* **2022,** *61* (10), e202115024.

5. Zheng, Y.; Han, X.; Cheng, P.; Jia, X.; Xu, J.; Bu, X. H., Induction of Chiral Hybrid Metal Halides from Achiral Building Blocks. *J. Am. Chem. Soc.* **2022,** *144* (36), 16471-16479.

6. Han, X.; Cheng, P.; Han, W.; Shi, R.; Guan, J.; Li, G.; Xu, J., Circularly polarized luminescence and nonlinear optical harmonic generation based on chiral zinc halides. *Chem. Commun.* **2023,** *59* (48), 7447-7450.

7. Han, X.; Cheng, P.; Shi, R.; Zheng, Y.; Qi, S.; Xu, J.; Bu, X. H., Linear optical afterglow and nonlinear optical harmonic generation from chiral tin(IV) halides: the role of lattice distortions. *Mater. Horiz.* **2023,** *10* (3), 1005-1011.

8. Li, B.; Yu, Y.; Xin, M.; Xu, J.; Zhao, T.; Kang, H.; Xing, G.; Zhao, P.; Zhang, T.; Jiang, S., Second-order nonlinear optical properties of copper-based hybrid organic-inorganic

perovskites induced by chiral amines. *Nanoscale* **2023,** *15* (4), 1595-1601.

9. Qi, S.; Ge, F.; Han, X.; Cheng, P.; Shi, R.; Liu, C.; Zheng, Y.; Xin, M.; Xu, J., 0D chiral hybrid indium(III) halides for second harmonic generation. *Dalton Trans.* **2022,** *51* (22), 8593-8599.

10. Guan, J. J.; Zheng, Y. S.; Cheng, P. X.; Han, W. Q.; Han, X.; Wang, P. H.; Xin, M. Y.; Shi, R. C.; Xu, J. L.; Bu, X. H., Free Halogen Substitution of Chiral Hybrid Metal Halides for Activating the Linear and Nonlinear Chiroptical Properties. *J. Am. Chem. Soc.* **2023,** *145* (49), 26833-26842.

11. Yu, B. Y.; Han, W. Q.; Liu, G. K.; Wei, Y. Y.; Wei, J.; Zheng, Y. S.; Dang, Y. Y., Oxidation-Induced Dissolution Recrystallization Structural Transformation Strategy Enhanced Nonlinear Optical Effect of Hybrid Chiral Tin Bromide Single Crystals. *Inorg. Chem.* **2023,** *62* (49), 20520-20527.

12. Qi, S.; Cheng, P.; Han, X.; Ge, F.; Shi, R.; Xu, L.; Li, G.; Xu, J., Organic–Inorganic Hybrid Antimony(III) Halides for Second Harmonic Generation. *Cryst. Growth Des.* **2022,** *22* (11), 6545-6553.

13. Zhao, L.; Han, X.; Zheng, Y.; Yu, M.-H.; Xu, J., Tin-Based Chiral Perovskites with Second-Order Nonlinear Optical Properties. *Adv. Photon. Res.* **2021,** *2* (11), 2100056.

14. Shen, C.; Sun, D.; Dang, Y.; Wu, K.; Xu, T.; Hou, R.; Chen, H.; Wang, J.; Wang, D., $(C_4H_{10}NO)PbX_3$ (X = Cl, Br): Design of Two Lead Halide Perovskite Crystals with Moderate Nonlinear Optical Properties. *Inorg. Chem.* **2022,** *61* (42), 16936-16943.

15. Wang, H.; Li, J.; Lu, H.; Gull, S.; Shao, T.; Zhang, Y.; He, T.; Chen, Y.; He, T.; Long, G., Chiral Hybrid Germanium(II) Halide with Strong Nonlinear Chiroptical Properties.

Angew. Chem. Int. Ed. **2023,** *62* (41), e202309600.

16. Guo, Z.; Li, J.; Wang, C.; Liu, R.; Liang, J.; Gao, Y.; Cheng, J.; Zhang, W.; Zhu, X.; Pan, R.; He, T., Giant Optical Activity and Second Harmonic Generation in 2D Hybrid Copper Halides. *Angew. Chem. Int. Ed.* **2021,** *60* (15), 8441-8445.

17. Xin, M.; Cheng, P.; Han, X.; Shi, R.; Zheng, Y.; Guan, J.; Chen, H.; Wang, C.; Liu, Y.; Xu, J.; Bu, X. H., Resonant Second Harmonic Generation in Proline Hybrid Lead Halide Perovskites. *Adv. Opt. Mater.* **2023,** *11*, 2202700.

18. Fu, D.; Xin, J.; He, Y.; Wu, S.; Zhang, X.; Zhang, X. M.; Luo, J., Chirality-Dependent Second-Order Nonlinear Optical Effect in 1D Organic–Inorganic Hybrid Perovskite Bulk Single Crystal. *Angew. Chem. Int. Ed.* **2021,** *60* (36), 20021-20026.

19. Fu, X. W.; Zeng, Z. X. S.; Jiao, S. L.; Wang, X. X.; Wang, J. X.; Jiang, Y.; Zheng, W. H.; Zhang, D. L.; Tian, Z. H.; Li, Q. Y.; Pan, A. L., Highly Anisotropic Second-Order Nonlinear Optical Effects in the Chiral Lead-Free Perovskite Spiral Microplates. *Nano Lett.* **2023,** *23* (2), 606-613.

20. Okada, D.; Araoka, F., Magneto-chiral Nonlinear Optical Effect with Large Anisotropic Response in Two-Dimensional Halide Perovskite. *Angew. Chem. Int. Ed.* **2024,** *63* (21), e202402081.

21. Guo, Z.; Li, J.; Liang, J.; Wang, C.; Zhu, X.; He, T., Regulating Optical Activity and Anisotropic Second-Harmonic Generation in Zero-Dimensional Hybrid Copper Halides. *Nano Lett.* **2022,** *22* (2), 846-852.

22. Guo, Z. H.; Li, J. Z.; Liu, R. L.; Yang, Y.; Wang, C. S.; Zhu, X.; He, T. C., Spatially Correlated Chirality in Chiral Two-Dimensional Perovskites Revealed by Second-

Harmonic-Generation Circular Dichroism Microscopy. *Nano Lett.* **2023,** *23*, 7434.